Additive Manufacturing 54 (2022) 102764

Contents lists available at ScienceDirect

Additive Manufacturing

journal homepage: www.elsevier.com/locate/addma

Advancing a real-time image-based jet lag tracking methodology for optimizing print parameters and assessing melt electrowritten fiber quality

Kai Cao, Fucheng Zhang, Ahmadreza Zaeri, Ralf Zgeib, Robert C. Chang *

Department of Mechanical Engineering, Stevens Institute of Technology, Hoboken, NJ 07030, USA

ARTICLE INFO

Keywords:
Melt electrowriting
Jet lag tracking
'Fiber pulsing'
Current leakage

ABSTRACT

Melt electrowriting (MEW) has emerged as an important additive manufacturing process to fabricate high-resolution microscale fibrous scaffolds for engineered tissue applications. However, the complex interplay between the numerous process variables renders parametric optimization of this additive manufacturing technique a challenging task. In order to facilitate the optimization of MEW-jetted fiber fabrication, this study adopts a real-time jet lag tracking methodology. Specifically, this methodology is implemented to determine the optimum conditions to improve the fiber quality featured by a prescribed mean diameter and an enhanced uniformity. Firstly, a serpentine toolpath is designed, and the real-time jet lag length signal is recorded, exhibiting multiple successive peaks. The coefficient of variance CV_{pv} correlated with these peak values is first identified as an indicator of the jet lag stability. Second, for a given pressure (P) and translational stage speed (v), as the applied voltage (U) increases, CV_{pv} is found to initially decrease before reaching a minimum point at $U{=}U_c$, followed by an increase at higher U values. U_c represents an inflection point on the graph of CV_{pv} as a function of U, whereby fiber pulsing is observed when $U < U_c$. Otherwise, an enhanced fiber uniformity is achieved at the expense of detectable current leakage when $U > U_c$. Moreover, at a given P, as v decreases, U_c deceases and plateaus at a value U_b. Furthermore, U_b is found to increase as P increases. These aforementioned dependencies are closely related to the mass equilibrium around the Taylor cone. Finally, based on these results, a systematic protocol is advanced to determine the appropriate P-U-v settings that enable an enhanced printed fiber quality.

1. Introduction

As a convergence of melt electrohydrodynamic process and additive manufacturing (AM) principles [1–3], melt electrowriting (MEW), has emerged as an important approach to fabricate high-resolution microscale fibrous scaffolds or porous three-dimensional structures with tunable microarchitectures [4,5]. Based on the appropriate selection of process variables and guided by design parameters, the MEW process enables complex scaffolds to be produced with heterogeneous features [6] and hierarchical structures [7,8]. Due to its facile implementation [9], solvent-free process [10], and high tunability [11,12], MEW has emerged as a promising AM approach for engineered tissue applications [13–16]. However, its process tunability towards precise, microscale geometries hinges on understanding the complex interplay between the numerous process variables that are highlighted by, but not limited to material temperature, pressure (P), voltage (U), translational stage speed (v), along with the most recently reported collector temperature [17,18]. In practice, the extent and nature of the interrelationships between the process variables introduce significant challenges to the optimization of MEW printing parameters [19,20]. This is further exacerbated by the varied MEW system configurations in terms of material heating and feeding methods [21]. Moreover, the geometrical dimensions of the MEW process variants also diverge with respect to the nozzle diameter, and collector size, etc.

In order to understand the manifold relationships between the various MEW process variables and the measurement outcomes, divergent methodologies have been adopted for MEW process parameterization. On one hand, Tourlomousis et al. applied dimensional analyses to establish a printability number as an indicator of printing quality [19]. On the other hand, Dayan et al. applied a response surface methodology to investigate the effect of different variables on fiber diameter [20]. In these studies, many of the process parameters are considered in tandem, requiring that numerous equations and experiments be taken into consideration. As a result, these approaches demand significant experimental design iterations without providing the needed intuitive or mechanistic insight into the MEW process physics. To address these

* Correspondence to: 1 Castle Point Hudson, Hoboken, NJ 07030, USA.
E-mail address: rchang6@stevens.edu (R.C. Chang).

https://doi.org/10.1016/j.addma.2022.102764
Received 23 June 2021; Received in revised form 10 January 2022; Accepted 10 March 2022
Available online 12 March 2022

drawbacks, an alternative approach would be to identify a traceable and responsive indicator of the process conditions, such as the jet lag. In terms of the precise indicator to evaluate the jet lag, one candidate is the jet lag length L, defined as the distance between the contact point of the jet and the projection point of the nozzle on the collector. Another candidate is the flightpath angle θ [22], which is determined by satisfying $tan\theta = \frac{L}{D}$, where D is the distance from the nozzle tip to the collector. The advancement and utilization of a jet lag tracking methodology would be advantageous in MEW parametric studies for several reasons. First, the jet lag can be precisely monitored with optical imaging in real time to reflect the printing stability. Furthermore, the observed jet lag is presumed to be sensitive to the change in various critical process variables, such as the voltage (U), the pressure (P), and the translational stage speed (v). However, the gap in understanding this onboard AM process measurement and its implications relates to how the jet lag tracking methodology can be implemented to improve fiber quality. Hochleitner et al. firstly noticed that 'fiber pulsing' (undesired sectional oscillation of fiber diameter) can be reflected in the fluctuation of jet lag [23]. This 'fiber pulsing' phenomenon has been observed for some other polymer materials [24,25]. Wunner et al. introduces the notion of printomics into an MEW parametric study, wherein the effects of various variables on θ and fiber diameter (d_f) are investigated [22]. Another example is the convergence of machine vision and MEW, where θ, Taylor cone area and fiber diameter are measured and correlated to improve the printing stability [26]. However, the rich information reflected in the jet lag variation in these studies were not fully extracted and utilized.

Based on these parametric studies, the interplay of different process variables has been partially revealed and incompletely understood. First, the translational stage speed (v) needs to be higher than a critical translational speed v_c [27] so that the liquid rope coiling phenomena can be avoided [28,29]. Second, the applied voltage (U) needs to exceed a critical value U_c, so that the 'fiber pulsing' phenomena (the undesired sectional oscillation of the fiber diameter) can be avoided [23]. However, although it is known that the elimination of 'fiber pulsing' indicates the achievement of U_c, how to exactly determine its value is still unknown. Moreover, a systematic methodology to evaluate jet lag stability and how the jet lag stability is related to the fiber uniformity, and more generally, the printing stability, is needed. Finally, an intuitive and effective protocol needs to be developed to facilitate the optimization of the MEW printing parameters.

Many of the aforementioned challenges and knowledge gaps are addressed in this study. Specifically, based on a real-time image-based jet lag tracking methodology for the MEW process, a new indicator of jet lag stability, the jet lag peak values' coefficient of variation, namely CV_{pv}, is introduced to optimize for the MEW measurement outcome of fiber uniformity. The effect on CV_{pv} of three key process variables, namely the applied pressure (P), the applied voltage (U), and the translational stage speed (v), are investigated. Furthermore, a protocol of parametric optimization based on jet lag tracking methodology is advanced to print fibers with prescribed mean fiber diameter and enhanced uniformity.

2. Materials and methods

2.1. Material preparation

Poly(ε-Caprolactone) (PCL) is in the form of pellets with a mean molecular weight of 45,600 g/mol, mass density of 1.021 g/mL, and polydispersity of 1.219 (Capa 6500, Perstop Ltd. Of UK). A 5 mL pneumatic syringe (Intellispence, Agoura Hills, CA, USA) is loaded with PCL pellets and placed in the heating oven (90 ℃) overnight with its needle-end upside. After each experiment, the syringe is kept at room temperature to avoid unnecessary thermal degradation.

2.2. MEW system configuration

The MEW system used in this study is schematized in Fig. 1. The pneumatic syringe loaded with PCL pellets is heated by a double-walled heating vessel made from alumina ceramics. Between the outer and inner walls of the heating vessels is a heating pad (New Era Pump Systems, Farmingdale, NY, USA) set at 105 ℃. The syringe is connected to an air dispenser (Intellispense, Agoura Hills, CA, USA), which can regulate its output air pressure. The nozzle of the syringe is connected to the positive terminal of a high voltage supply (Stanford Research Systems, Sunnyvale, CA, USA), while the grounded negative terminal is connected to the collector plate through an autoranging picoammeter (9103 USB, RBD Instruments, OR, USA) by a BNC cable. The collector plate (203 mm × 203 mm×3.3 mm, shown in Fig. 1) is fixed on an alumina block as an insulator and the alumina block is mounted on an XY moving platform consisting of two slides (Velmex, USA) driven by step motors. The ambient temperature is kept at 23.5 ± 1 ℃. The key parameters enabling the MEW process are listed in Table 1.

2.3. Imaging and data measurement

An inverted motorized microscope (IX83, Olympus, USA) along with its imaging processing software (CellSens 2.11) is used to image and characterize all samples. A 20 × objective lens with a magnification set at 12.6 is adopted for all samples. For all the data, three sampling points are measured, and the mean is taken as the result. A 1080 P, 60FPS, industry microscope camera with 0.5 × to 4.5 × objective (Lapsun, CN) is positioned suitably to take the high-resolution images and videos of the printing process as shown in Fig. 1. The mass of samples is measured by a high precision electronic balance (HFS FA204, California, USA). All the temperatures are measured with a thermometer (Traceable 4039, USA).

2.4. Jet lag tracking and algorithm of jet lag length calculation

To enable the jet lag tracking methodology, a real-time identification of jet location and calculation of the jet lag length is required. First, a pure blackboard is used as the background and the lighting condition is adjusted to increase the contrast between the jet and the background. Second, the obtained video frames from the camera are grayed and binarized with a careful selection of binarization threshold. A schematic of the binary image is shown in Fig. 2a (For display convenience, the color is inverted i.e., the nozzle, jet and the scaffold should be white but is shown in black in the schematic, while the background should be black but is shown in white in the schematic). Since the jet is not uniformly bright, its outline in the binary picture is sometimes discontinuous (Fig. 2a). Third, the white pixels representing the jet are searched for to determine the jet location and calculate the jet lag. For each frame in the video, the following steps are taken to calculate the jet lag length.

(1) The pixel points are scanned for their values row by row from the top to the bottom of the picture. For the first several rows, the x coordinate of the first white point encountered does not change since it represents the left edge of the nozzle. And the number of white pixels D_{noz} represents the outer diameter of the nozzle (D_{noz} is determined to be 11 for all experiments).
(2) Keep scanning the pixel points until the x coordinate of first white pixel point encountered changes compared to the previous rows. The coordinate of this pixel point P_{upper} represents the upper location of the jet (Fig. 2a). Once P_{upper} is determined, terminate the top-to-bottom scanning process.
(3) Start scanning the pixel points row by row from bottom to top, until a row is found, in which only several continuously adjacent white points can be identified. And the amount of these points should not exceed a threshold D_{jet} representing the maximum possible diameter of the jet (D_{jet} is tried and set at 20). The

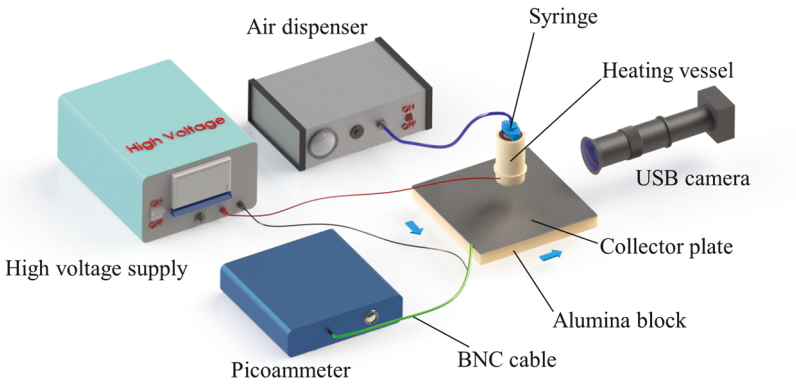

Fig. 1. Schematic of MEW system.

Table 1
The parameters and their values or range in the MEW process.

Parameters	Values
Heating pad set temperature	105 °C
Voltage (U)	10–19 kV
Pressure (P)	7.5–17.5 psi
Tip-to-collector distance (D)	20 mm
Inter-fiber distance	1 mm
Translational stage speed (v)	10–20 mm/s

location of the first white point P_{lower} is identified as the lower location of the jet.

(4) The jet lag length is calculated as $L = 0.82\frac{|x(P_{lower}) - x(P_{upper})|}{D_{noz}}$ (mm). 0.82 is the outer diameter of the nozzle in millimeters.

As is shown in Fig. 2b, the serpentine toolpath applied for jet lag tracking includes lots of translation segments in succession, whose length is defined as travel length. For each travel in the toolpath, the jet lag length signal is recorded, and the peak value of the signal during a travel is extracted for further data processing. To avoid the interference between the adjacent travels, the stage will pause for a specified duration, namely dwelling time, at each dwelling point shown in Fig. 2b.

3. Results

The focus of this study is to investigate the effects of some key process variables on the single-fiber uniformity by image-based tracking of the jet lag, which is a traceable indicator of how far the jet deposition lags from the nozzle in real time. This will enable the advancement of a systematic protocol to identify the optimum process conditions under which an enhanced fiber uniformity can be achieved.

3.1. Effects of voltage, translational stage speed, and pressure on the mean output flow rate

The evaluation of single fiber quality involves two metrics, namely the mean fiber diameter $\overline{d}_f$ and the fiber uniformity. This section will focus on the control of $\overline{d}_f$. Before doing so, it is necessary to make a distinction between the material flow rate from the syringe barrel to the Taylor cone (namely input flow rate or Q_{in}) and the material flow rate out of the Taylor cone (namely output flow rate or Q_{out}). Under specified conditions (i.e., P, U, v, and other conditions are specified), Q_{in} is thought to be constant, while Q_{out} may fluctuate with time. If the polymer melt is assumed to be incompressible, the mean output flow rate over a sufficiently long duration, namely the mean output flow rate ($\overline{Q}_{out}$), is expected to be equal to Q_{in}. In this way, it can be surmised that the mean fiber diameter $\overline{d}_f$ is determined by the mean flow rate ($\overline{Q}_{out}$) and v ($\overline{d}_f = \sqrt{\frac{4\overline{Q}_{out}}{\pi v}}$ with the assumption that the deposited fiber is circular in cross section and barely deformed due to the impact between the jet and collector). However, the dependency of $\overline{Q}_{out}$ on other process variables such as P, U and v has not been previously investigated. To study the dependency of $\overline{Q}_{out}$ on v, P and U are fixed at 10 psi and 14 kV, respectively and v is toggled between 0 (stationary), 5, 10, 15 and 20 mm/s. Moreover, to examine the dependency of $\overline{Q}_{out}$ on U, P is fixed at 10 psi and the stage is kept stationary, while U is varied at 10, 12.5, 15, 17.5 and 20 kV. Finally, to investigate the effect of P on $\overline{Q}_{out}$, U is fixed at 15 kV and the stage is kept stationary, while P is toggled between 7.5, 10, 12.5, 15 and 17.5 psi. Based on these experimental design parameters, $\overline{Q}_{out}$ is ascertained by measuring the mass of material deposited on the collector over a 15-minute duration. The rationale for

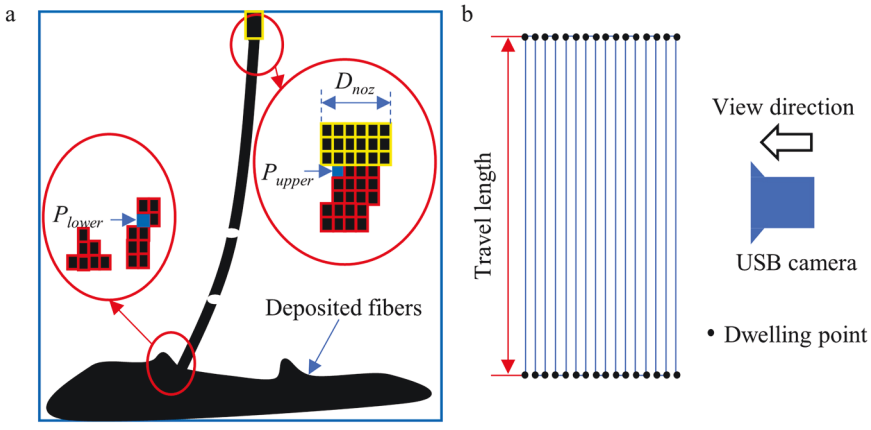

Fig. 2. Schematic of jet lag tracking. (a) schematic of the algorithm for jet lag tracking. The profile of the nozzle is circumscribed in yellow rectangle. And the pixel points corresponding to the nozzle is also circumscribed in yellow rectangles. D_{noz} denotes the number of pixel points representing the outer diameter of the nozzle; P_{upper} and P_{lower} denote the pixel points identified as the location of the upper and lower tips of the jet, respectively. The deposited fibers may be unevenly distributed on the collector, thus forming a wavy curve representing their profile. (b) the serpentine toolpath for jet lag tracking. Black points denote the dwelling points, where the stage pauses for a designed period, namely dwelling time. The view direction of the camera is perpendicular to the direction of each translation segment in the toolpath.

selecting this time duration for material collection and measurement is determined by the scale of the repetition period of the jet lag waveform, as shown in a subsequent section (Section 3.3). By implementing this experimental procedure, the results are illustrated in Fig. 3 which plots $\overline{Q}_{out}$ versus P, U, and v variables. $\overline{Q}_{out}$ is found to increase with increasing P, and be invariant with v and U.

3.2. Effect of voltage on fiber uniformity at a constant translational stage speed and pressure

Since the preceding results show that $\overline{Q}_{out}$ depends solely on P, if P and v are specified, the measured mean or nominal $\overline{d}_f$ value will be equal to the prescribed value. On the other hand, the remaining challenge of fiber quality control is how to improve the fiber uniformity as reflected by minimizing fluctuations in d_f. To investigate the effect of voltage (U) on fiber uniformity, v and P are kept at 18 mm/s and 10 psi, respectively, and U is increased from 10 kV to 19 kV with an increment of 1 kV. To characterize the fiber uniformity, the range of d_f, defined as the difference between the maximum and minimum values for d_f, is introduced. To be clear, the range, instead of the standard deviation of d_f, is used here since the latter metric is unsensitive to local significant deterioration of fiber uniformity. Specifically, the determination of fiber diameter range is based on observation and multipoint sampling. This is enabled by selecting the fiber segments observably thicker or thinner than the rest, and then making the measurement at more than 3 points for each segment to find the extreme value. The range of d_f at different voltages U are measured in Fig. 4a and the microscopic images of fibers at 10 kV and 15 kV are shown in Fig. 4b-c. From Fig. 4a, as U increases, the range of d_f significantly decreases from 325 μm at 10 kV to 6.6 μm at 15 kV and remains at a low level for higher voltages. At low voltages (<15 kV), some fiber segments significantly thicker than others can be observed (solid rectangle in Fig. 4b and e), indicating the existence of 'fiber pulsing', while some of other fiber segments are strained bordering on breakage (dashed rectangle in Fig. 4b and d). By contrast, fibers printed at 15 kV show an enhanced uniformity (Fig. 4c).

3.3. Effect of voltage on the jet lag waveform at a constant translational stage speed and pressure

Based on the previous studies [23], the fluctuation of the fiber diameter, namely 'fiber pulsing', is closely related to the fluctuation of jet lag. Since the voltage (U) is found to significantly affect the fiber uniformity, it should also affect the jet lag stability. The conditions applied are the same as those in Section 3.2 for data comparability. As shown in Fig. 5a-f, the jet lag signal is composed of many peaks in succession, each of which corresponds to a travel in the toolpath. The peak values are recorded as the jet lag length for the corresponding translation segment. To evaluate the magnitude and fluctuation of jet lag, three statistical quantities, are calculated for peak values measured in 150 s, including the standard deviation (STD_{pv}), the average (AVG_{pv}), and the coefficient of variation (CV_{pv}= STD_{pv} /AVG_{pv}). From Fig. 5a-c, the evolution of the jet lag waveform indicates that at low levels of U (10–14 kV), the evolution of peak values shows periodicity. Each period starts with a peak whose amplitude is significantly higher than that of the previous adjacent peak, such as Peak A and Peak B in Fig. 5b. In this way, the time duration elapsed between Peak A (included) and Peak B (excluded) constitutes a complete repetition period. In each period, the peak value overall decreases with time. As U increases, both STD_{pv} and AVG_{pv} decrease steadily (Fig. 5g-h), while CV_{pv} decreases to a minimum value at 15 kV and then increases (Fig. 5i). In this way, at a specific P and v (which enable a specific $\overline{d}_f$), U_c can be found to achieve a minimum CV_{pv}. In addition to CV_{pv}, another feature of the waveform of interest is the repetition period. Based on the results in Fig. 5j, it is shown that the repetition period decreases with U. Since the longest repetition period is around 70 s, $\overline{Q}_{out}$, calculated from the material deposited over a 15-minute duration, is a good approximation of the actual mean output flow rate (Fig. 3).

3.4. Effects of translational stage speed on the plot of CV_{pv} vs. U at a constant pressure

It is known that jet lag can be observed when the translational stage speed v is high enough and that the jet lag length increases as v increases. Yet, the effect of v on the jet lag fluctuation has not been investigated. In this section, P is kept at 10 psi, and v is toggled from 10 to 20 mm/s with an increment of 2 mm/s. For each level of v, the voltage U is increased from 10 kV with an increment of 1 kV until, at a high U, the jet lag is not observable. The dependence of CV_{pv} on U is plotted at different v levels, as shown in Fig. 6a. It is indicated that the shapes of the plot are similar at different v, however, U_c increases when v is high (14–20 mm/s, shown in Fig. 6b). When v does not exceed 14 mm/s, U_c is almost fixed at 13 kV. Therefore, for a specific value of P, it is possible to determine a minimum U_c when v is small enough, which is termed the basic critical voltage, U_b (as shown in the red dashed rectangle in Fig. 6b).

3.5. Effects of pressure on U_b

Since the minimum U_c, namely U_b, can be found at a fixed P based on Section 3.4, it is possible to find the dependency of U_b on P. In this section, P is increased from 7.5 psi to 17.5 psi with an increment of 2.5 psi. For each level of P, v is decreased from 14 to 6 mm/s with a decrement of 0.25 mm/s. At each P and v, U is increased from 10 kV with an increment of 0.25 kV. Results in Sections 3.3 and 3.4 are used here to avoid unnecessary experiments. Based on the dependency of CV_{pv} on U (Fig. 5i), at each P and v, after each attempt of the different values of U, CV_{pv} is calculated promptly. When CV_{pv} starts to increase with U, this means the last attempted value of U is U_c. Moreover, based on the dependency of U_c on v (Fig. 6b), at each P, if v is small enough that

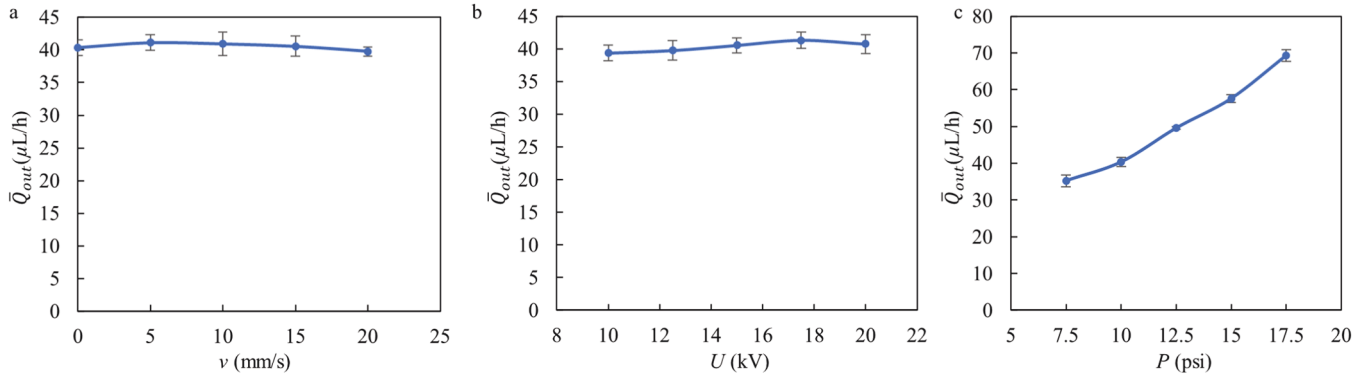

Fig. 3. Effects of the translational stage speed v (a), the applied voltage U (b) and the applied pressure P (c) on the mean output flow rate $\overline{Q}_{out}$.

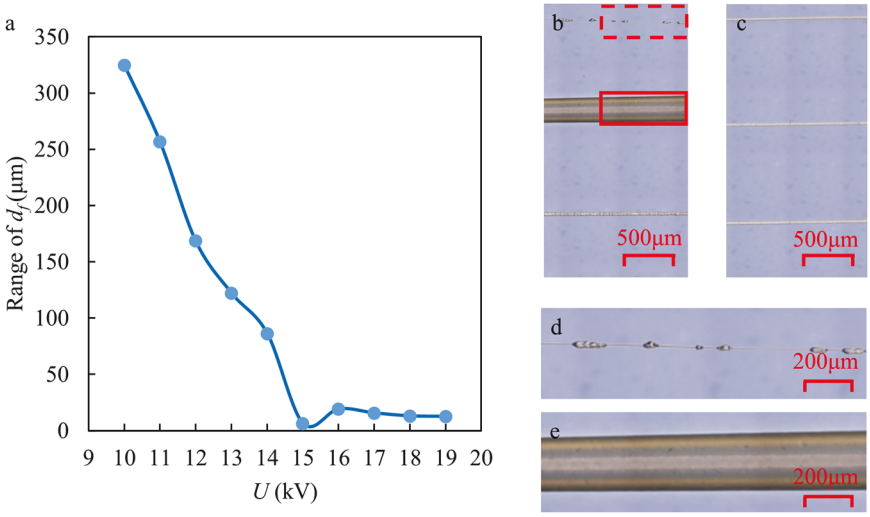

Fig. 4. Dependence of fiber uniformity on U (P: 10 psi, v: 18 mm/s, travel length: 50 mm, dwelling time: 1 s): (a) dependence of the range of d_f on U. (b-c) microscopic image of fibers printed at 10 and 15 kV, respectively. The solid rectangle in b shows a fiber segment with a significantly larger d_f than others; the dashed rectangle in b shows a fiber segment bordering on breakage. By contrast, fibers printed at 15 kV in (c) shows an enhanced uniformity. (d) and (e) are the magnification of the dashed and solid rectangular part in (a).

U_c starts to be invariant with v, this indicates that the current U_c is U_b. In this way for each P, U_b is found. The dependency of U_b on P is shown in Fig. 6c. Moreover, for each P, the critical translational stage speed at the corresponding U_b, namely the basic critical stage speed, v_b, decrease from 8.25 mm/s at 7.5 psi to 6.5 mm/s at 17.5 psi. Based on the dependency of $\overline{Q}_{out}$ on P in Fig. 3c, the fiber diameter, d_{fb}, at each P, U_b, and v_b, can be calculated and measured as shown in Fig. 6d.

4. Discussion

Broadly speaking, the quality of an MEW-enabled scaffold can be evaluated at two levels, namely its constituent fibers and its three-dimensional structure. On one hand, at the single-fiber level, two metrics of fiber quality, the mean and variation of the fiber diameter d_f [23], are closely related to the studied process variables, including the applied voltage (U), translational stage speed (v), and applied pressure (P), which are extensively investigated in this paper. On the other hand, at the three-dimensional structural level, the fidelity by which the fibers are assembled into a typical scaffold is beyond the scope of this study.

The quality of a fiber is evaluated by $\overline{d}_f$ and the fiber uniformity as measured by the fiber diameter range. It can be understood that $\overline{d}_f$ is a function of $\overline{Q}_{out}$ and v. Since v can be prescribed, the only undetermined variable here is $\overline{Q}_{out}$. Fortunately, $\overline{Q}_{out}$ is found to be independent of U and v as demonstrated in Fig. 3. In this way, $\overline{d}_f$ can be tuned conveniently by adjusting the applied pressure P and v. Compared to the control of $\overline{d}_f$, tuning the fiber uniformity is more challenging, as it requires real-time monitoring during the MEW process. To enable in-process monitoring, a conveyor belt has been used by others to move the printed fibers to an imaging module [22]. However, this method requires intermittent operation of the process. To address this limitation, the jet lag is tracked to reflect the printing stability and the uniformity of the deposited fibers.

4.1. Relationship between the fluctuation of Taylor cone volume, jet lag length, and fiber diameter

The rationale for the jet lag tracking methodology assumes that the improvement of the jet lag stability is accompanied by that of the fiber uniformity [26]. However, this is true only when the jet lag fluctuation is caused by a voltage specification that falls below the threshold value. As will be shown later, a random jet lag fluctuation can be initiated at an exceedingly high voltage. If it is assumed that the voltage falls below the threshold value, the relationship between the fluctuation of the Taylor cone, jet lag and fiber diameter is illustrated in Fig. 7 and explained as follows.

Specifically, Fig. 7a schematizes the evolution of an unstable printing process when $U < U_c$, which is accompanied by the fluctuation of the Taylor cone and jet lag. Since U is so low that the output flow rate (Q_{out}) from t_0 to t_2 is lower than the input flow rate Q_{in}, the volume of the Taylor cone (V_{TC}) steadily increases. Furthermore, since the inflight jet segment close to the contact point is characterized by a relatively small diameter for this duration (from t_0 to t_2), a parallel phenomenon inferred is that this portion of the inflight jet segment is sufficiently accelerated by the electric force. As a result of jet acceleration, the difference between the jet speed and v becomes less insignificant. Therefore, the jet lag length is maintained at a relatively low value from $t = t_0$ to $t = t_2$. However, when V_{TC} increases to a critical value, a beaded jet segment (red circumscribing dashed lines at t_3) will arise from a displaced portion of the Taylor cone and experience elongation owing to the combined effects of the electric force and mechanical stretching force during the deposition process. Concomitantly, V_{TC} rapidly decreases to a smaller value at t_3 than the previous instants. As shown at t_3, the inflight jet is largely occupied by the beaded jet segment (large in diameter), therefore, the moment of inertia of the inflight jet with respect to the vertex of the Taylor cone (point O at t_3), I_O, is relatively large compared to previous time instants. Since there are no significant changes in the moment of the stretching force with respect to point O, M_O, it is more difficult for M_O to drag the jet from the vertical direction considering the large I_O at t_3. Therefore, the jet lag at t_3 is the smallest among these time instants of interest. Moreover, the electric force is unable to effectively accelerate the beaded jet segment considering its large mass. Once the leading tip of the beaded jet segment contacts the collector, due to the large difference between the jet speed and v, the stretching force as well as L rapidly becomes significant at t_4. This stretching force will be exerted on the subsequent part of the inflight beaded segment, which results in its fast landing without a sufficient thinning process. Additionally, the stretching force will be also exerted on the material following the beaded jet segment, which results in an ultrathin trailing jet segment (blue dashed circumscribing lines). After the beaded jet segment has been completely deposited since the subsequent trailing jet segment is sufficiently accelerated by the electric force and the stretching force, the difference between the jet speed and v becomes less significant, resulting in the decrease of jet lag at t_5 compared to t_4.

By analyzing the fluctuation of V_{TC} and L, it is now feasible to understand the fluctuation of the fiber diameter d_f. From t_0 to t_3, d_f does not deviate from the prescribed value significantly, while the deposited fiber segment corresponding to the beaded jet segment shown at t_4 is characterized by a significantly larger d_f. Subsequently, an ultrathin fiber segment corresponding to the trailing jet segment is deposited on the

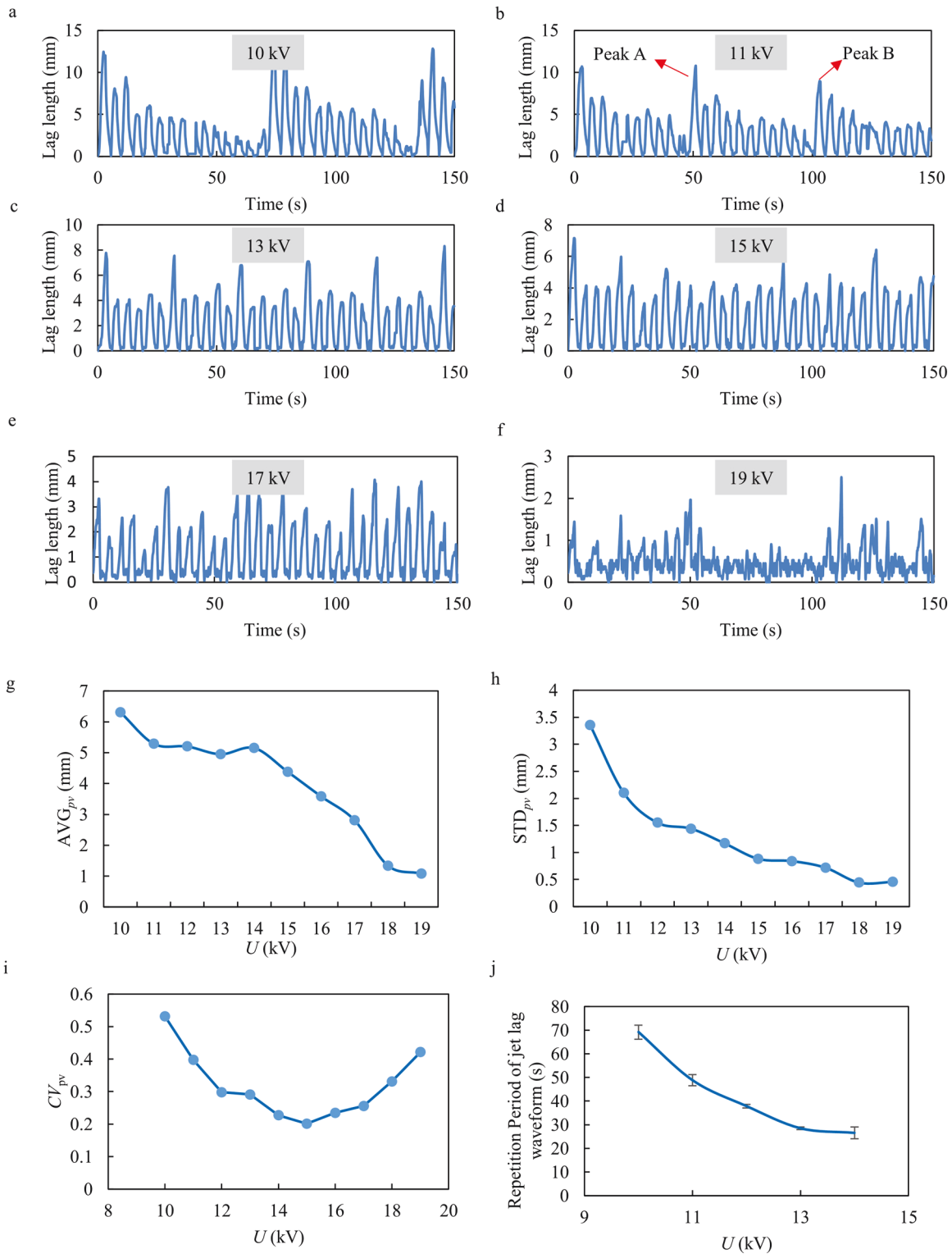

Fig. 5. Effect of U on jet lag. (a-f) Jet lag waveform at different U. (g-j) Dependence of AVG$_{pv}$, STD$_{pv}$, CV_{pv}, repition period on U. P: 10 psi, v: 18 mm/s, travel length: 50 mm, dwelling time: 1 s. Since AVG$_{pv}$, STD$_{pv}$, CV_{pv} are the statistical results of many sample points in a duration, there are no error bars for these plots.

collector at t_5. Therefore, when $U < U_c$, any fluctuations observed in the printing process, including the fluctuations of V_{TC}, L, and d_f are representations of the same printing instability at different phases of material deposition. Specifically, the printing instability is represented by the fluctuation of V_{TC} around the nozzle, then by the fluctuation of jet lag length for the inflight jet, and finally by the fluctuation of fiber diameter after deposition.

Of these three fluctuations, the fiber diameter fluctuation with time can be reflected by the variation of the printed fiber diameter with the deposition location. Moreover, the in-process fluctuation of jet lag can be tracked in real time and is the focal methodology of this study. In contrast, the fluctuation of V_{TC} with time is difficult to determine. Due to the unsteady nature of the 'fiber pulsing' phenomena, the volumetric flow rate measured at any cross section along the jet is not necessarily

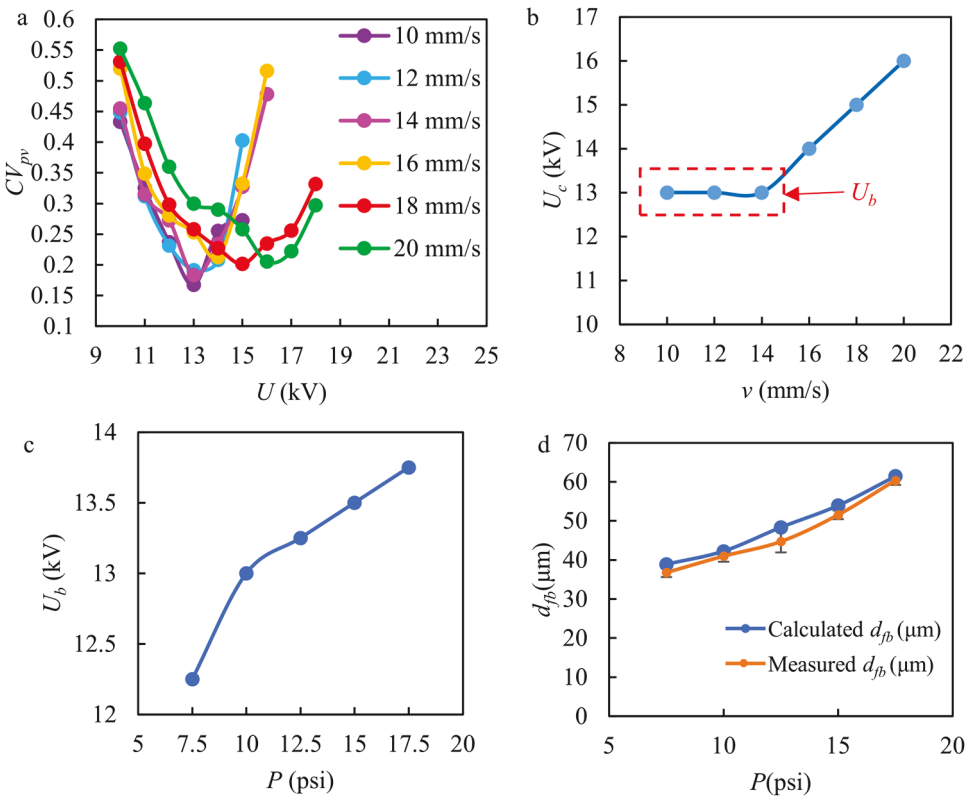

Fig. 6. Effects of v and P on jet lag fluctuation: (a) Effects of v on the plot of CV_{pv} vs. U at a fixed P (10 psi); (b) Dependence of U_c on v at a P (10 psi). P:10 psi, travel length: 50 mm, dwelling time: 1 s. For the portion of the plot circumscribed by the red dashed rectangle, U_c is fixed at U_b when $v \leq 14$ mm/s. (c-d) Dependence of U_b (c) and d_{fb} (d) on P (travel length: 50 mm, dwelling time: 1 s).

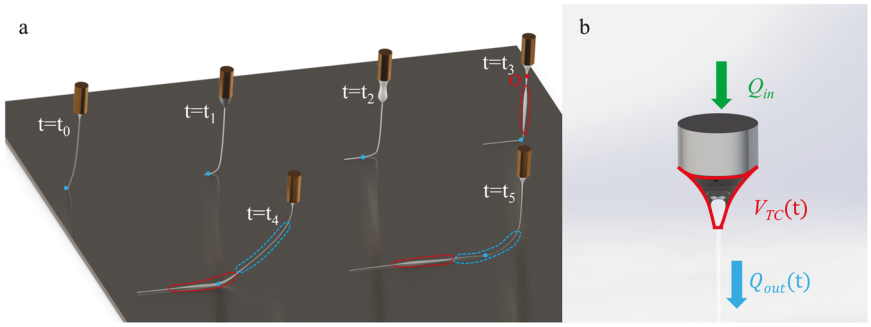

Fig. 7. Fluctuation of the Taylor cone volume (V_{TC}), jet lag length (L), and fiber diameter (d_f). (a) schematizes the evolution of a dynamic unstable printing process from $t = t_0$ to $t = t_5$ under fixed conditions (i.e., P, U, and v are kept constant). The red circumscribing dashed lines denote the beaded jet segment and the blue circumscribing dashed lines denote the trailing jet segment. The blue points denote the contact point of the jet on the collector at each time instant. The red point O denotes the vertex of the Taylor cone at $t = t_3$. (b) shows the definition of Q_{in}, Q_{out}, and V_{TC}.

constant with time and location. Therefore, it is difficult to determine the instantaneous Taylor cone volume without directly measuring it. Apparently, a direct volume measurement is infeasible, yet it might be possible to calculate V_{TC} by imaging its outline and determining its cross-sectional area [26] if it is axisymmetric. However, this method is invalidated by the irregular (i.e., non-axisymmetric) Taylor cone shape, which is exacerbated when it is stretched due to a significant jet lag. Despite these difficulties, it is possible to theoretically analyze different flow rates around the Taylor cone as formulated in Eq. (1) and based on a mass equilibrium approach.

$$Q_{in} = \frac{dV_{TC}}{dt} + Q_{out} \tag{1}$$

where Q_{in} denotes the flow rate of material extruded out of the nozzle and depends solely on P. V_{TC}(t) denotes the dynamic volume of the Taylor cone illustrated in Fig. 7b. Q_{out} denotes the flow rate of material drawn out of the Taylor cone. Considering the periodicity of the flow rate fluctuation, Eq. (1) can be integrated from $t = 0$ to $t = \tau$, where τ is the repetition period of fluctuation.

$$\int_0^\tau Q_{in}dt = \int_0^\tau \frac{dV_{TC}}{dt}dt + \int_0^\tau Q_{out}dt$$

Since Q_{in} depends solely on P, and Taylor cone returns to its initial shape after a whole period, Eq. (2) can be derived as follows. Based on Eq. (2), Q_{out} fluctuates around its integral mean, which equals Q_{in}.

$$\int_0^\tau \frac{dV_{TC}}{dt}dt = 0 \quad \text{therefore,} \quad Q_{in} = \frac{1}{\tau}\int_0^\tau Q_{out}dt \tag{2}$$

Based on the previous discussion which establishes the correlations between fluctuations of the Taylor cone volume V_{TC}, jet lag length L, and fiber diameter d_f, the following sections will start with discussing the validity of CV_{pv} as an indicator of jet lag stability. Then, the effect of U on the jet lag stability evaluated by CV_{pv} will be discussed, in which the significance of U_c is clarified. Finally, the effects of P and v on U_c are understood by analyzing the flow rate fluctuation around the Taylor

cone.

4.2. Significance of CV_{pv} as an indicator of jet lag stability

To evaluate the jet lag stability, an effective indicator needs to be found. The standard deviation of jet lag length, STD_{pv} is not a good candidate for the following reason. It can be understood that when U is too high, the sparking phenomenon is likely to happen, which brings significant instability to the jet lag. However, the steady decrease in STD_{pv} with U implies that the jet lag appears to be more stable at high voltages (Fig. 5h). This contradiction in the dependency of jet lag stability on U originates from the fact that when U is altered, the jet speed is also altered. Specifically, if the translational stage speed v is kept constant, the difference between the jet speed and v will be changed. In this way, the jet lag signals are scaled up or down as a function of this difference. This scaling effect invalidates the evaluation of jet lag stability by way of STD_{pv} metrics. As a more intuitive description, based on a statistical formulation, it can be assumed that U has no effect on the jet lag stability (which is not experimentally true), whereby the jet lag signal at a high voltage is represented by a random variable X. The expectation and standard deviation of X are μ_{pv} and σ_{pv}, respectively. Then the jet lag signal at a relatively low voltage should be represented by another random variable $Y = kX$, where $k > 1$, meaning that the jet lag signal is scaled up considering that the difference of jet speed and v is more significant. Therefore, the expectation and standard deviation of Y should be $k\mu_{pv}$ and $k\sigma_{pv}$, respectively. In this way, even though the jet lag stability is the same for these two assumed cases (i.e., high and low voltage), the standard deviation of Y is larger than that of X. Based on this understanding, a steady decrease in STD_{pv} with U in Fig. 5h does not necessarily imply that the jet lag stability is steadily improving. To eliminate the aforementioned scaling effect, the coefficient of variation, $cv_{pv} = \mu_{pv}/\sigma_{pv}$, is introduced to evaluate the jet lag stability. With the new metric introduced, the jet lag stability is the same for the assumed two cases, which is consistent with the assumption that U has no effect on the jet lag stability. Statistically, μ_{pv} and σ_{pv} are estimated by AVG_{pv} and STD_{pv}, respectively. Therefore, CV_{pv}, defined as STD_{pv}/AVG_{pv}, is used to estimate cv_{pv}. By plotting CV_{pv} as a function of U (Fig. 5i), U_c can be found to achieve a minimal CV_{pv} representing an optimized jet lag stability condition.

4.3. Effects of voltage on jet lag stability

Based on the significance of CV_{pv}, it is now feasible to analyze the dependence of jet lag stability on other process variables. Specifically, for a given P and v, when U increases, CV_{pv} initially decreases to a minimum point at U_c and then increases for higher U levels. As is shown in Fig. 5a-c, when $U < U_c$, the jet lag waveform shows periodicity, resulting in a relatively large CV_{pv} and deterioration of jet lag stability. For Fig. 5d-f when $U > U_c$, there will be a corona discharge between the nozzle and the collector plate, resulting in detectable current leakages (shown in Fig. 8). For this experiment (i.e., current leakage measurement), the initial U is set at 9 kV and increased by 1 kV every 1 min. The stage is kept stationary because the stage translation will induce additional undesired current signals. On one hand, it is observed that at low U levels (9–12 kV), the current signal is characterized by the low-amplitudes-but-high-frequency fluctuations, which can be regarded as the background noise. On the other hand, when U is 13 kV or higher, notable high-amplitudes-but-low-frequency fluctuations arise on the current signal, which indicates the existence of current leakage. It should be noted that except for a zero v, all the other process parameters in this experiment are comparable to those shown in Fig. 6a-b. Considering U_c tends to be invariant when v is small in Fig. 6b, it is reasonable to extrapolate that when the stage is stationary, U_c is 13 kV. The current leakage causes a temporary disruption of the electric field and results in a random fluctuation of jet lag length, thus the increase of CV_{pv} when $U > U_c$.

After analyzing the relationship between the fluctuation of jet lag and fiber uniformity as well as the effect of U on the CV_{pv}, it is now possible to understand that when $U < U_c$, the fluctuation of jet lag and fiber uniformity are both the representations of the same printing instability, while when $U > U_c$, they are not correlated anymore. This explains the dependencies of CV_{pv} and range of d_f on U are similar when $U < U_c$, but different when $U > U_c$ (Figs. 4a and Fig. 5i).

4.4. Effects of pressure and translational stage speed on U_c

The effect of pressure and translational stage speed on U_c can be understood by analyzing their effects on the mass equilibrium around the Taylor cone. As is stated before, a stable Taylor cone requires equivalent and constant Q_{in} and Q_{out}, which requires a proper pressure P and a sufficiently high voltage U. Compared to the fundamental parameters P and U, the translational stage speed v is an auxiliary parameter for keeping the mass equilibrium since this equilibrium can be maintained even without the stage translation. When the stage is stationary, for a specific Q_{in}, there exists a basic critical voltage, U_b (for example 13 kV in Fig. 6b), which is high enough to stably draw the material out of the Taylor cone at an equal Q_{out}. If U is lower than U_b, the 'fiber pulsing' will always happen (regardless of the translational stage speed v). Therefore, U_b can be defined as the minimum U_c to enable a steady Taylor cone at a specific Q_{in}, which is determined by P, and therefore, is a function of it, $U_b(Q_{in})$ or $U_b(P)$. Since higher P implies higher Q_{in} (Fig. 3c), U_b increases with P (Fig. 6c). At U_b, the speed of the material at the contact point of the jet with the collector, or the jet speed, can be determined by gradually increasing v to a critical value when the liquid rope coiling disappears, and a straight fiber can be printed. This critical translational stage speed is defined as the basic critical translational stage speed, v_b. Therefore, $U = U_b$ and $v = v_b$ forms the basic conditions to print a straight uniform fiber. Since U_b is the minimum U_c and v_b determined at U_b is the minimum v_c, the fiber diameter printed under basic conditions, d_{fb}, is the maximum possible fiber diameter at a specific P.

Given the aforementioned basic conditions, when v is increased slightly from v_b, the stretching force due to stage translation is not strong enough to affect Q_{out}. Therefore, U_c is invariant (equal to U_b) with v in this case (such as v<14 mm/s in Fig. 6b). When v exceeds a critical value and the stretching force is strong enough to significantly affect Q_{out}, the material equilibrium near the Taylor cone is disrupted and the fluctuation of Q_{out} will arise. To eliminate this fluctuation, U_c needs to be increased so that the jet speed can be increased, which in turn, alleviates the jet lag and weakens the stretching force. Consequently, Q_{out} returns to a stable value equal to Q_{in} and the fluctuation disappears. This explains the dependency of U_c on v in Fig. 6b. In summary, U_c is a function of both U_b and v and can be expressed as U_c ($U_b(P)$, v) or U_c (P, v).

The analysis about the effects of process parameters on U_c clearly

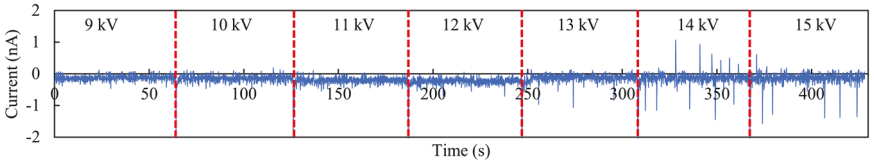

Fig. 8. Current leakage at different U levels on stationary collector plates.

shows that the printing instability can be initiated by disrupting either Q_{in} (by increasing P) or Q_{out} (by increasing v) in Eq. (1). In contrast, the increase of U helps to inhibit the printing instability by maintaining a stable Q_{out} equal to Q_{in} and enabling a relatively high jet speed.

4.5. Protocol to print fibers with a desirable mean fiber diameter and enhanced uniformity

The methodology of jet lag tracking for the MEW process provides not only a powerful way to monitor printing instability, but also a protocol for parametric optimization, as is shown in Fig. 9.

Step 1: From the graph of d_{fb} as a function of P, for each prescribed fiber diameter $\hat{d}_f$, a corresponding minimum usable pressure, P_{min} can be obtained (Fig. 9 upper left picture). The parameter P is prescribed at a value slightly higher than P_{min} and $\overline{Q}_{out}$ is determined based on the plot of $\overline{Q}_{out}$ with respect to P.

Step 2: The translational stage speed $v = \frac{4\overline{Q}_{out}}{\pi \hat{d}_f^2}$ is set based on the prescribed fiber diameter $\hat{d}_f$ and $\overline{Q}_{out}$.

Step 3: An arbitrary U value is prescribed, and the printing process is initiated whereby the jet lag is tracked throughout the printing process. Whenever there is periodic jet lag fluctuation, U is increased. If U is too high wherein the sparking phenomenon is initiated, the printing process is terminated.

As a simple verification of the proposed protocol, if the prescribed fiber diameter, $\hat{d}_f$ is 50 μm, from the graph of d_{fb} as a function of P, P_{min}= 14.39 psi. Therefore, P can be set at 15 psi, which is slightly higher than P_{min}. To precisely determine the corresponding output flowrate, the deposited fibers are collected on the stationary collector

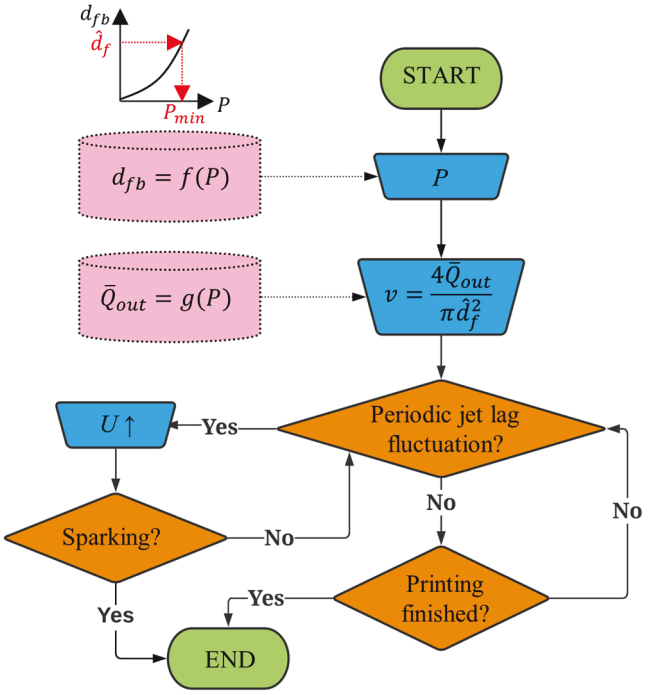

Fig. 9. Flow chart of the protocol of printing fibers with a prescribed mean fiber diameter and superior uniformity. The blue trapezoidal nodes denote the steps where the *P-U-v* settings need adjustment. The orange diamond nodes denote the steps where decision-making is required based on observation. The pink cylindrical nodes denote the database ready to use, including the dependencies of d_{fb} and $\overline{Q}_{out}$ on P. d_{fb} denotes the fiber diameter printed under the basic conditions at a specific P. $\overline{Q}_{out}$ denotes the mean output flow rate. $\hat{d}_f$ denotes the prescribed fiber diameter. v is the translational stage speed calculated from a given $\overline{Q}_{out}$ and $\hat{d}_f$.

and U is set at 18 kV to preclude 'fiber pulsing', and $\overline{Q}_{out}$ is determined to be 65.8 μL/h. In this way, $v = \frac{4\overline{Q}_{out}}{\pi \hat{d}_f^2} = 9.3$ mm/s. When printing with the serpentine toolpath is initiated at U= 11 kV, periodic fluctuation of jet lag can be clearly observed (blue curve in Fig. 10a) with a significant fluctuation in fiber diameter (Fig. 10b). When the parameter U is increased to 12 kV, the jet lag fluctuation is much less significant (orange curve in Fig. 10a), and some high peaks occasionally arise. To accelerate the optimization process, U is increased by 2–14 kV, and jet lag fluctuation is not observable (grey curve in Fig. 10a) while the peaks exhibit uniformity. The fiber morphologies are shown in Fig. 10c, which exhibit a desired fiber diameter (around 50 μm) and an enhanced uniformity.

Herein, the proposed protocol provides a convenient way for parametric optimization in MEW process, yet several points need to be mentioned regarding its implementation. First, the efficiency of the protocol is based on the acquirement of enough data about the investigated MEW system, including the dependencies of $\overline{Q}_{out}$ and d_{fb} as a function of P. Secondly, to enable the protocol, the material property, material temperature and ambient conditions cannot be changed significantly. Otherwise, the abovementioned dependencies may fail to work. Third, to precisely obtain a prescribed fiber diameter, it is recommended to determine $\overline{Q}_{out}$ each time before the optimization process. To decrease the time duration required to collect the deposited fibers for mass measurement, U can be set at a relatively high value to preclude the 'fiber pulsing'. Finally, the protocol may fail to address printing of a relatively high-layered scaffold (more than 200 layers), whereby the residual charge accumulation becomes problematic [18]. Due to this, the jet lag becomes increasingly significant, which can introduce periodic jet lag fluctuation caused by the stretching force of the stage. In extreme cases, it is likely that the jet lag fluctuation can't be eliminated by increasing U. Lastly, the applicability of the protocol needs to be tested for other materials.

5. Conclusions

In this study, a parametric investigation is implemented for a microscale AM technique, namely the MEW process, based on the jet lag tracking methodology. The fluctuation of the Taylor cone volume V_{TC}, jet lag length L, and fiber diameter d_f are thought to be the representations of the same printing instability at different phases. First of all, $\overline{Q}_{out}$ is found to depend solely on P and does not change with U and v. Therefore, $\overline{d}_f$ can be determined for a specific P and v. If they are specified, U_c can be found to achieve a minimal CV_{pv}, which is identified as an indicator for jet lag stability. When $U < U_c$, the 'fiber pulsing' exists, and the jet lag waveform shows periodicity. While when $U < U_c$, an enhanced fiber uniformity can be achieved at the expense of detectable current leakage. Under specific pressure P, U_c is initially fixed at U_b, then increases as v increases. Furthermore, U_b is found to increase as P increases.

For further considerations, CV_{pv} is an important indicator of the jet lag stability, while U_c is an important variable for improving the fiber uniformity when $\overline{d}_f$ is fixed at a given P and v. However, when analyzing the mechanism through which v affects the mass equilibrium around the Taylor cone, and thus the fiber uniformity, it is important to notice that when the jet lag length is large, a significant stretching force due to the stage translation is the culprit for the deterioration of fiber uniformity. Therefore, if the jet lag length is observed to increase for other reasons, such as the cumulative residual charge when the layer number is large for high-layered scaffold printing [18,30–32], the fiber uniformity may deteriorate (Fig. S1). In this case, U is recommended to be increased to overcome the jet lag instability and ensure an enhanced fiber uniformity. The determination of U_c as a function of layer number is a promising direction of this study and more broadly reports on the significance of process tunability of MEW as it emerges as a promising AM

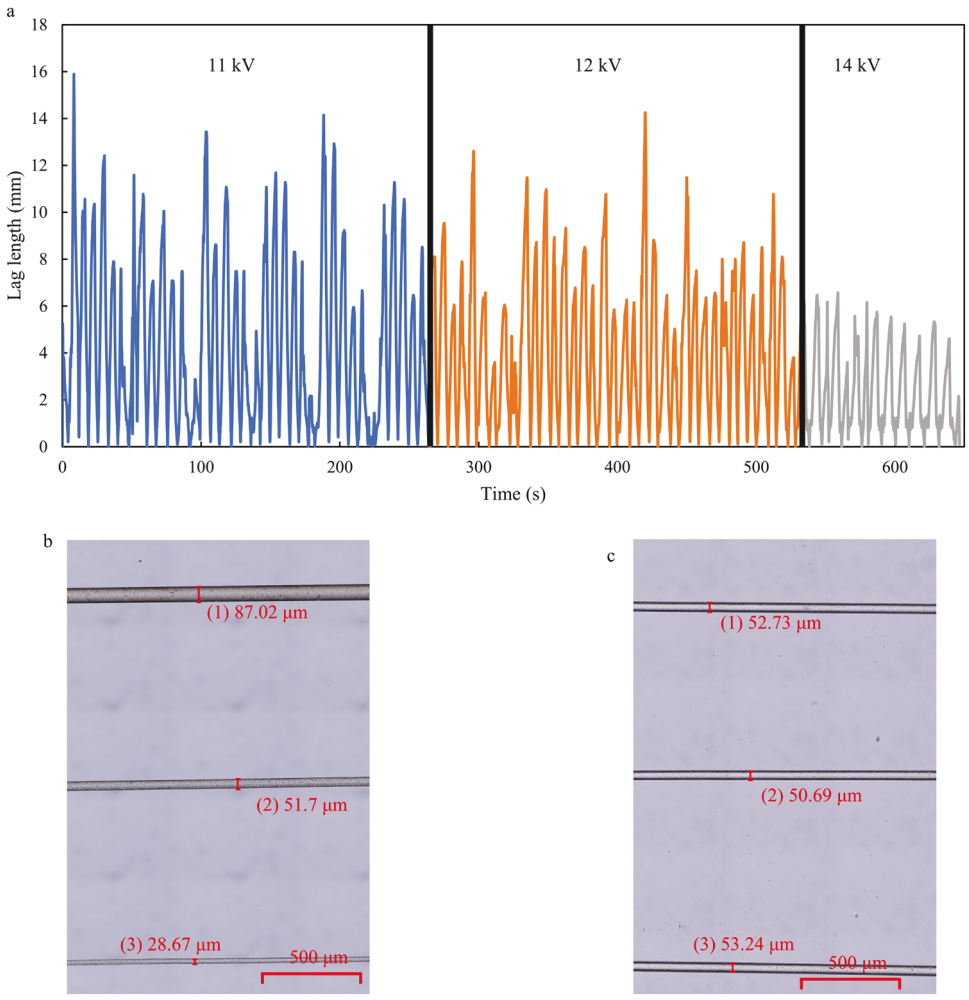

Fig. 10. Implementation of the proposed protocol under the task of printing fiber with a prescribed diameter of 50 μm. *P*:15 psi, travel length: 50 mm, dwelling time: 1 s, *v*: 9.3 mm/s. *U* is increased from 11 kV to 14 kV. (a) the jet lag waveform at different voltage values. (b) and (c) show the fiber morphologies printed at 11 kV and 14 kV, respectively.

approach for engineered tissue applications [33].

Funding

The research was funded by the National Science Foundation under Award No. CMMI-MME-1663095 and the U.S. Army Medical Research and Development Command under Award No. USMRAA-W81XWH-19-1-0158. Any opinions, findings, and conclusions or recommendations expressed in this publication are those of the authors and do not necessarily reflect the views of the National Science Foundation or the U. S. Army Medical Research Acquisition Activity.

CRediT authorship contribution statement

Kai Cao: Conceptualization, Methodology, Software, Validation, Formal analysis, Investigation, Data curation, Writing – original draft, Visualization **Robert C. Chang:** Conceptualization, Methodology, Resources, Writing – review & editing, Supervision, Project administration, Funding acquisition **Fucheng Zhang:** Conceptualization, Software, Writing – review & editing **Ahmadreza Zaeri:** Validation, Visualization, Writing – review & editing **Ralf Zgeib:** Formal Analysis, Visualization, Writing – review & editing.

Declaration of Competing Interest

The authors declare that they have no known competing financial interests or personal relationships that could have appeared to influence the work reported in this paper.

Appendix A. Supporting information

Supplementary data associated with this article can be found in the online version at doi:10.1016/j.addma.2022.102764.

References

[1] S.M. Giannitelli, P. Mozetic, M. Trombetta, A. Rainer, Combined additive manufacturing approaches in tissue engineering, Acta Biomater. 24 (2015) 1–11, https://doi.org/10.1016/j.actbio.2015.06.032.
[2] J.C. Kade, P.D. Dalton, Polymers for melt electrowriting, Adv. Healthc. Mater. 10 (2021), https://doi.org/10.1002/adhm.202001232.
[3] G. Constante, I. Apsite, H. Alkhamis, M. Dulle, M. Schwarzer, A. Caspari, A. Synytska, S. Salehi, L. Ionov, 4D biofabrication using a combination of 3D printing and melt-electrowriting of shape-morphing polymers, ACS Appl. Mater. Interfaces (2021), https://doi.org/10.1021/acsami.0c18608.
[4] Q. Chen, X. Mei, Z. Shen, D. Wu, Y. Zhao, L. Wang, X. Chen, G. He, Z. Yu, K. Fang, D. Sun, Direct write micro / nano optical fibers by near-field melt electrospinning, Opt. Lett. 42 (2017) 5106–5109.
[5] I. Liashenko, A. Hrynevich, P.D. Dalton, Designing outside the box: unlocking the geometric freedom of melt electrowriting using microscale layer shifting, Adv. Mater. 32 (1–6) (2020), 2001874, https://doi.org/10.1002/adma.202001874.

[6] Y. Jin, Q. Gao, C. Xie, G. Li, J. Du, J. Fu, Y. He, Fabrication of heterogeneous scaffolds using melt electrospinning writing: Design and optimization, Mater. Des. 185 (2020), 108274, https://doi.org/10.1016/j.matdes.2019.108274.
[7] Y. Su, Z. Zhang, Y. Wan, Y. Zhang, Z. Wang, L.H. Klausen, P. Huang, M. Dong, X. Han, B. Cui, M. Chen, A hierarchically ordered compacted coil scaffold for tissue regeneration, NPG Asia Mater. 12 (2020) 4–13, https://doi.org/10.1038/s41427-020-0234-7.
[8] A. Hrynevich, S. Bilge, J.N. Haigh, R. Mcmaster, A. Youssef, C. Blum, T. Blunk, G. Hochleitner, J. Groll, P.D. Dalton, Dimension-based design of melt electrowritten scaffolds, Small 14 (2018), 1800232, https://doi.org/10.1002/smll.201800232.
[9] T.D. Brown, P.D. Dalton, D.W. Hutmacher, Melt electrospinning today: an opportune time for an emerging polymer process, Prog. Polym. Sci. 56 (2016) 116–166, https://doi.org/10.1016/j.progpolymsci.2016.01.001.
[10] H. Lian, Z. Meng, Melt electrospinning vs. solution electrospinning: a comparative study of drug-loaded poly (ε-caprolactone) fibres, Mater. Sci. Eng. C. 74 (2017) 117–123, https://doi.org/10.1016/j.msec.2017.02.024.
[11] T.M. Robinson, D.W. Hutmacher, P.D. Dalton, The next frontier in melt electrospinning: taming the jet, Adv. Funct. Mater. 29 (2019), 1904664, https://doi.org/10.1002/adfm.201904664.
[12] A. Abdal-hay, N. Abbasi, M. Gwiazda, S. Hamlet, S. Ivanovski, Novel polycaprolactone/hydroxyapatite nanocomposite fibrous scaffolds by direct melt-electrospinning writing, Eur. Polym. J. 105 (2018) 257–264, https://doi.org/10.1016/j.eurpolymj.2018.05.034.
[13] M. Castilho, D. Feyen, M. Flandes-Iparraguirre, G. Hochleitner, J. Groll, P.A. F. Doevendans, T. Vermonden, K. Ito, J.P.G. Sluijter, J. Malda, Melt electrospinning writing of poly-hydroxymethylglycolide-co-ε-caprolactone-based scaffolds for cardiac tissue engineering, Adv. Healthc. Mater. 6 (2017) 1–9, https://doi.org/10.1002/adhm.201700311.
[14] P.B. Warren, Z.G. Davis, M.B. Fisher, Parametric control of fiber morphology and tensile mechanics in scaffoldswith high aspect ratio geometry produced via melt electrowriting formusculoskeletal soft tissue engineering, J. Mech. Behav. Biomed. Mater. 99 (2019) 153–160, https://doi.org/10.1016/j.jmbbm.2019.07.013.
[15] M. Castilho, A. van Mil, M. Maher, C.H.G. Metz, G. Hochleitner, J. Groll, P. A. Doevendans, K. Ito, J.P.G. Sluijter, J. Malda, Melt electrowriting allows tailored microstructural and mechanical design of scaffolds to advance functional human myocardial tissue formation, Adv. Funct. Mater. 28 (2018) 1–10, https://doi.org/10.1002/adfm.201803151.
[16] B. Huang, E. Aslan, Z. Jiang, E. Daskalakis, M. Jiao, A. Aldalbahi, C. Vyas, P. Bártolo, Engineered dual-scale poly (ε-caprolactone) scaffolds using 3D printing and rotational electrospinning for bone tissue regeneration, Addit. Manuf. 36 (2020), 101452, https://doi.org/10.1016/j.addma.2020.101452.
[17] J.N. Haigh, T.R. Dargaville, P.D. Dalton, Additive manufacturing with polypropylene microfibers, Mater. Sci. Eng. C. 77 (2017) 883–887, https://doi.org/10.1016/j.msec.2017.03.286.
[18] K. Cao, F. Zhang, A. Zaeri, R. Zgeib, R.C. Chang, A charge-based mechanistic study into the effect of collector temperature on melt electrohydrodynamic printing outcomes, Adv. Mater. Technol. (2021), 2100251, https://doi.org/10.1002/admt.202100251.
[19] F. Tourlomousis, H. Ding, D.M. Kalyon, R.C. Chang, Melt electrospinning writing process guided by a "printability number", J. Manuf. Sci. Eng. 139 (2017), 081004 https://doi.org/10.1115/1.4036348.
[20] C.B. Dayan, F. Afghah, B.S. Okan, M. Yıldız, Y. Menceloglu, M. Culha, B. Koc, Modeling 3D melt electrospinning writing by response surface methodology, Mater. Des. 148 (2018) 87–95, https://doi.org/10.1016/j.matdes.2018.03.053.
[21] M.L. Muerza-Cascante, D. Haylock, D.W. Hutmacher, P.D. Dalton, Melt electrospinning and its technologization in tissue engineering, Tissue Eng. Part B Rev. 21 (2015) 187–202, https://doi.org/10.1089/ten.teb.2014.0347.
[22] F.M. Wunner, P. Mieszczanek, O. Bas, S. Eggert, J. Maartens, Printomics: the high-throughput analysis of printing parameters applied to melt electrowriting, Biofabrication 11 (2019), 025004, https://doi.org/10.1088/1758-5090/aafc41.
[23] G. Hochleitner, A. Youssef, A. Hrynevich, J.N. Haigh, T. Jungst, J. Groll, P. D. Dalton, Fibre pulsing during melt electrospinning writing, BioNanoMaterials 17 (2016) 159–171, https://doi.org/10.1515/bnm-2015-0022.
[24] A. Nadernezhad, M. Ryma, H. Genç, I. Cicha, T. Jüngst, J. Groll, Melt electrowriting of isomalt for high-resolution templating of embedded microchannels, Adv. Mater. Technol. 6 (2021), https://doi.org/10.1002/admt.202100221.
[25] G. Hochleitner, J.F. Hümmer, R. Luxenhofer, J. Groll, High definition fibrous poly (2-ethyl-2-oxazoline) scaffolds through melt electrospinning writing, Polym. (Guildf.) 55 (2014) 5017–5023, https://doi.org/10.1016/j.polymer.2014.08.024.
[26] P. Mieszczanek, T.M. Robinson, P.D. Dalton, D.W. Hutmacher, Convergence of machine vision and melt electrowriting, Adv. Mater. (2021), 2100519, https://doi.org/10.1002/adma.202100519.
[27] G. Hochleitner, F. Chen, C. Blum, P.D. Dalton, B. Amsden, J. Groll, Melt electrowriting below the critical translation speed to fabricate crimped elastomer scaffolds with non-linear extension behaviour mimicking that of ligaments and tendons, Acta Biomater. 72 (2018) 110–120, https://doi.org/10.1016/j.actbio.2018.03.023.
[28] G. Hochleitner, F. Chen, C. Blum, P.D. Dalton, B. Amsden, J. Groll, Melt electrowriting below the critical translation speed to fabricate crimped elastomer scaffolds with non-linear extension behaviour mimicking that of ligaments and tendons, Acta Biomater. 72 (2018) 110–120, https://doi.org/10.1016/j.actbio.2018.03.023.
[29] W.E. King, G.L. Bowlin, Near-field electrospinning and melt electrowriting of biomedical polymers—progress and limitations, Polymers 13 (2021) 1097, https://doi.org/10.3390/polym13071097.
[30] H. Ding, K. Cao, F. Zhang, W. Boettcher, R.C. Chang, A fundamental study of charge effects on melt electrowritten polymer fibers, Mater. Des. 178 (2019), 107857, https://doi.org/10.1016/j.matdes.2019.107857.
[31] K. Cao, F. Zhang, R.C. Chang, A charge-based mechanistic study into the effects of process parameters on fiber accumulating geometry for a melt electrohydrodynamic process, Processes 8 (2020) 1440, https://doi.org/10.3390/pr8111440.
[32] F.M. Wunner, M. Wille, T.G. Noonan, O. Bas, P.D. Dalton, E.M. De-juan-pardo, D. W. Hutmacher, Melt electrospinning writing of highly ordered large volume scaffold architectures, Adv. Mater. 30 (2018), 1706570, https://doi.org/10.1002/adma.201706570.
[33] R. Chen, R.C. Chang, B. Tai, Y. Huang, B. Ozdoganlar, W. Li, A. Shih, Biomedical manufacturing: a review of the emerging research and applications, J. Manuf. Sci. Eng. 142 (2020), 110807, https://doi.org/10.1115/1.4048043.